Journal of Applied Research and Technology

www.jart.icat.unam.mx

ICAT Instituto de Ciencias Aplicadas y Tecnología

Journal of Applied Research and Technology 24 (2026) 619-631

Original

Simultaneous Double Emission of Blue-Cyan Light from Europium Nanostructures in a Solid Host

Lothar José Carlos Vilchis-Martínez[1*] • Elsi Violeta Mejía-Uriarte[1*]
Roberto Ysacc Sato-Berrú[1] • Oleg Kolokoltsev[1] • Naser Qureshi[1]
Iván Gómez-Arista[2] • Dwight Acosta-Najarro[3] • Enrique Camarillo-García[3]

[1]Instituto de Ciencias Aplicadas y Tecnología, Universidad Nacional Autónoma de México, Circuito Exterior S/N, Ciudad Universitaria, 04510, Mexico City, Mexico.
[2]SECIHTI - Instituto Nacional de Astrofisica, Óptica y Electrónica (INAOE), Luis Enrique Erro #1, Tonanzintla, 72840 San Andrés Cholula, Puebla, Mexico.
[3]Instituto de Física, Universidad Nacional Autónoma de México, Circuito de la Investigación Científica S/N, Ciudad Universitaria, 04510, Mexico City, Mexico.

Received: 25 02 2025; Accepted: 24 09 2025
Available: 31 08 2026

Abstract: A sample of potassium bromide, doped with divalent europium ions, was stored at 200 $°C$ for approximately six months and exhibited two emission bands at room temperature: blue and cyan. These emissions are associated with two types of nanostructures (NS) that form during annealing. The localized emission spectra were obtained in a scanning zone (SZ) 46×162 μm^2 from a selected sample of 900×320 μm^2 and 90 μm in thickness using an experimental light-scanning design implemented in our laboratory. While scanning the crystal, several changes in the peak position and intensity of the emission spectra were observed. These changes corresponded to the stable dihalide phase (SDP) and the metastable dihalide phase (MDP). In certain regions, the intensity of the cyan emission band was slightly more significant than that of the blue emission band. The concurrent observation of these two emission bands confirms the coexistence of both phases within the single crystal.

Keywords: **Spectra emission, , luminescent nanostructures, double emission, stable dihalide phase metastable dihalide phase.**

*Corresponding authors.
E-mail address: lothar.vilchis@icat.unam.mx (L.J.C. Vilchis-Martinez), elsi.mejia@icat.unam.mx (E. Mejía-Uriarte).
Peer Review under the responsibility of Universidad Nacional Autónoma de México.

1. Introduction

Numerous research teams, including ours, have investigated divalent europium in solid host-type alkaline halides (Hernández et al., 1980; Muñoz-Santiuste et al., 1990; Pérez-Salas et al., 1996; Mejía-Uriarte et al., 2003). Its high luminescent efficiency and simple host make it an ideal subject for testing how the europium ion responds to different crystalline environments (López et al., 1980; da Cunha Andrade et al., 2014; de Carcer et al., 1988). In recent years, research has also focused on how systems, such as $KBr{:}Eu^{2+}$ (Mejía-Uriarte et al., 2009), $NaCl{:}Mn^{2+}$ (Mejía-Uriarte et al., 2015), and $NaCl{:}Cd^{2+}$ (Barth & Henry, 2009), configure within nanostructures (NS) in the host. When the impurities are precipitated, form impurity-vacancy (I-V) complexes that are grouped into structures of variable size, shape, and composition. These structures modify the optical properties of the material and are known as NS due to their nanoscale dimensions. As a phosphorus material, divalent europium continues to attract significant interest in previous and recent research. Its versatility is evident in its current applications, which range from LEDs to electronic devices (Hernández et al., 1980; Hossain et al., 2021; Luo et al., 2021), due to its high efficiency and strong chemical affinity for binding with various compounds. Some notable applications include scintillator materials, X-ray scintillators (Wu et al., 2016; Stand et al., 2019; Zhao et al., 2023; Zhang et al., 2024), and a single-crystal scintillator for detecting UV (Nikl & Yoshikawa, 2015). Halide Perovskites have strong blue emission, and lead-free metal halide nanocrystals are also gaining attention (Qiao et al., 2022; Huang et al., 2020). The emission of divalent europium has been reported as a single emission band due to the interconfigurational transition $4f^6 5d^1 \rightarrow 4f^7$ (Weakliem, 1972; Dorenbos, 2003; Duan & Reid, 2003; Qin et al., 2017). Recent publications have reported the observation of chemiluminescence in blue and green, obtained from the oxidation of organoaluminium compounds by oxygen in tetrahydrofuran (Galimov et al., 2020). A double emission of divalent europium was obtained in a solid solution, which can be used as a temperature sensor (Wu et al., 2019). Green emission in hydride chloride at low temperatures ($10 - 30\ K$), and perovskites with double emission violet and orange were reported (Kunkel et al., 2015; Yuan et al., 2024). In alkali halides, temperature and storage time are crucial for the formation of different phases within the crystal. Divalent europium ions in a solid alkali halide matrix tend to form one or more phases, depending on temperature and storage time. $200\ ℃$, a phase known as the dihalide phase (DP) $EuBr_2$ took place. For example, Eu^{2+} ions in KBr (Aguilar et al., 1982; Muñoz-Santiuste et al., 1990), KCl (López, 1981), and $NaBr$ (López et al., 1981) form one stable dihalide phase and two metastable phases, except for KBr, which has one stable dihalide phase (SDP) and one metastable dihalide phase (MDP).

For the sample $KBr{:}EuBr_2$ in bulk, the emission band peaking at $429.8\ nm$ was associated with the SDP $EuBr_2$, while that peaking at $466.2\ nm$ was to the MDP $EuBr_2$. To date, the $KBr{:}Eu^{2+}$ single crystal has not been examined by X-ray and electron microscopy techniques. However, the $NaCl{:}EuCl_2$ system for which these studies have been performed suggests that the SDP and MDP emission bands $EuBr_2$ can be assigned in accordance with those of $EuCl_2$. It should be noted that for this system, there is one band in SDP and two bands in MDP, assigned to the $[111]$, and $[310]$ planes of the matrix lattice. Another consideration for making this assignment is that the dihalide structure $EuCl_2$ should not be so different from $EuBr_2$. For precipitated phases, the $Eu^{2+}{-}Eu^{2+}$ distance will be greater in this sample, which allows the transfer of energy (Stepien-Damm & Dubiel, 1980; Eick & Smeggil, 1971).

When the sample is scanned step-by-step and luminescence is collected, the intensity of the emission bands changes along the way. These intensity changes are related to the thickness of the NS and its quantity. Thus, the intensity depends on the number of excited emitting ions. Peak shift of the emission band of the sample in SDP and/or MDP could be related to the diameter of the NS found at each point and to the collective emission of all of them. A similar behavior was reported in this same type of sample, but with NS formed in another phase. There, it was reported that the shift of the emission peak was a function of the NS diameter, which depends on the amount of europium impurities (Mejía-Uriarte et al., 2009).

Here, the purpose has been to study localized luminescence and determine the relationship between the emission band position and the NS in each phase. Although this material had been previously studied, its optical response had always been analyzed in volume, presenting a broad emission band with an asymmetric shape, and its component bands had only been determined by a deconvolution analysis. However, there has not yet been a report of well-defined double simultaneous emission spectra for this material.

2. Materials and Methods

The single crystals used in this work were grown using the Czochralski method. This technique has been used

to produce all the crystals in our research on alkaline halides doped with rare-earth or transition-metal ions (Hernández et al., 1980; Mejía-Uriarte et al., 2003; López et al., 1980). The $KBr{:}Eu^{2+}$ samples were heated in a furnace at $550 \pm 5°C$ for one hour and then rapidly cooled in liquid nitrogen. This process aims to dissolve any precipitated or aggregated phases that may have formed during crystal growth and to evenly distribute the europium ions within the crystal. The state of impurities dissolved in the host is commonly known as the state of free dipoles (FD). The samples were stored in a furnace at $200 \pm 5°C$ for six months to form the DP. These samples contain $\sim 240\ ppm$ europium ions; the calculation was performed using the method reported previously (Hernández et al., 1980). The sample measurements were $6\ x\ 3\ mm^2$ with $1\ mm$ in thickness and cut with a precision knife to obtain micro-samples. A total of ten microsamples were selected, with sizes ranging from hundreds of microns in area to several microns in thickness. The emission spectrum for each selected sample were analyzed, and the sample with the best asymmetric emission distribution was chosen (Kuzmin et al., 2024). This selected sample measures $900 \times 320\ \mu m^2$ with $90\ \mu m$ in thickness, and the scanning zone (SZ) was $46 \times 162\ \mu m^2$. The absorption spectra were obtained in bulk with a spectrophotometer (Cary 5000, Agilent), and emission spectra in bulk and localized mode were collected using a spectrometer (HR-2000+, Ocean Optics) calibrated to the line of an argon laser $514.5\ nm$. Annealing forms nanostructures through aggregation and precipitation. The area exhibiting the most intense cyan emission was selected for light scanning to acquire its image and emission spectra. Furthermore, the same region on the $[100]$ planes were examined using contact mode with Atomic Force Microscopy (AFM) (AutoProbe CP, Park Scientific Instruments) to obtain AFM images. To analyze and obtain 2D and 3D images, the open source software Gwyddion and WSxM 4.0 Develop 12.21 (Nečas & Klapetek, 2012; Horcas et al., 2007) were used. The images and luminescence spectra were acquired using a step-by-step light-scanning method, which is briefly summarized herein, as it is not the primary focus of this paper.

For the far-field regime, an objective microscope was used to capture the image and emission spectrum simultaneously. Figure 1 illustrates the experimental setup, where a digital camera (Industrial Camera, Thincol) is utilized to locate the sample position by detecting its reflection, thereby facilitating the identification of the area of interest. A laser beam with a wavelength of 375 nm (KVANT, $75mW$, TEM00, ND4116 LD, Niquia) is focused through a microscope objective (CFI plan Achromat NCG,

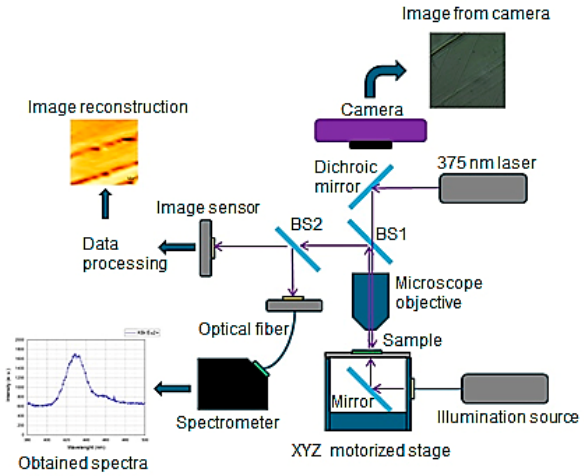

Figure 1. Experimental setup of *step-by-step* light scanning. BS 1. Beamsplitter 50/50 and BS 2. Beamsplitter 70/30.

100X, NA 0.9, Nikon) concentrating the laser beam onto the sample positioned on an XY platform (MT1/M) and Z (MVS05/M), with step motors (ZFS13) and controllers (KST201), these devices was acquired of Thorlabs Inc.

The fluorescence emitted from the sample is collected using the same microscope objective, with the light being channeled to both detection systems. A portion of the emitted light is used to form an image for data processing, while another is sent to the spectrometer for further analysis. The *step-by-step* light scanning method involves the absorption, reflection, and scattering of incident light on the sample. Irregularities on the surface of the sample create a correlation between the incoming and the reflected light. Differences in intensities enhance contrast, resulting in a clearer and more defined image. The photodiode is activated by the light emitted from the sample, and employing a Data Acquisition (DAQ USB 6343, NI) device in conjunction with LabView software 2024 Q1 (Licensed), variations in voltage are transformed into a data matrix. They are subsequently processed to generate a corresponding image.

Figure 2 (a) presents the selected micro-sample, characterized by a rectangular shape with certain irregularities. Using a stereoscopic microscope (T670-PL-NL040, AMSCOPE), a picture was taken with a digital camera (DCU224C-BG, Thorlabs) of the microsample under illumination from an LED light $365\ nm$ (M365L2, 700 mA, Thorlabs), which allowed the observation of fluorescence emitted by europium ions. The entire sample was scanned by micron steps, which facilitated the identification of an area exhibiting higher intensity within the emission spectrum with an asymmetric Gaussian distribution. This area

was subsequently selected for the *step-by-step* light scanning method, with intervals of 92 nm for each step, as illustrated in Figure 2 (b). Feature Generation and Regression (FGR) from Royerlab/Aydin (Solak et al., 2022) was employed to effectively eliminate noise from the image, a machine learning technique designed to enhance image sharpness and clarity. Additionally, the Python PINK sequential color map, as implemented with Matplotlib, was utilized, which provides a smooth transition from light to dark colors. This feature is handy for highlighting different data ranges within a single visualization. SZ displays a detailed view of the crystal surface, highlighting the defined growth terraces of the crystal and the irregularities present on its surface.

In Figure 3, the corresponding absorption spectra obtained over the entire micro-sample. Figure 3(a) presents the absorption spectra in the FD state after having been subjected to a heat treatment at 550 °C for one hour to dissolve the precipitated impurities, and the DP (stored for six months at 200 °C). Absorption spectra show significant differences between them. For FD state, the high-energy band is observed at $250.9 \pm 2\,nm$, while the low-energy band appears at $344.33 \pm 2\,nm$. The separation energy between them is a measure of the $10Dq$ splitting of the $5d$ orbitals by the crystal field into the e_g and t_{2g} levels, corresponding to a value of $10814.60 \pm 288\,cm^{-1}$ In contrast, the sample examined in DP shows a high-energy band at $275 \pm 2\,nm$ and a low-energy band at $333.5 \pm 2\,nm$, with a $10Dq$ value of $6378.62 \pm 169.30\,cm^{-1}$. The value of $10Dq$ decreased in $\sim 4435.98\,cm^{-1}$, when the sample is in the DP. The $4f \rightarrow 5d$ transitions are highly sensitive to the surrounding chemical environment; as can be seen, the high-energy band of the DP absorption spectrum has a strong red shift. These significant changes are attributed to the new phases in the crystal. These phases alter the local symmetry, thereby affecting the crystal field splitting of the $5d$ electron (Poort et al., 1997; Henderson & Imbusch, 2006). Figure 3(b) shows the second derivative of the FD and DP absorption spectra, where the structure of both bands can be seen more easily. This analysis helps to resolve overlapping absorption bands and improve the detection of changes in the crystalline environment. This approach enables a more refined examination of the spectral structure, revealing a clearer distinction between the two spectra (López et al., 1980; Aguilar et al., 1982) [5,29].

Figure 4 shows the emission spectrum of the entire microsample in FD (fuchsia line), DP (black line), and the convolution fit (red line). We analyze the full width at half maximum (FWHM) of the emission spectrum of the samples. The FD (impurity-vacancy dipoles and small

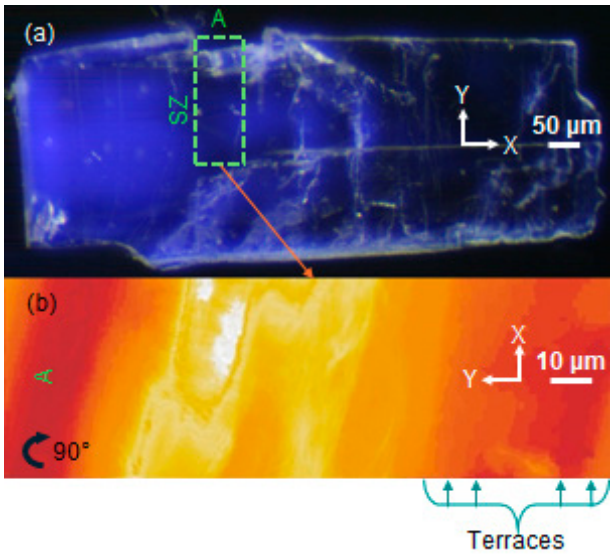

Figure 2. a) Micro-sample of KBr: Eu^{2+} ($900 \times 320\,\mu m^2$, 90 µm thickness). b) SZ, Imagen in 2D obtained by light scanning *step-by-step* ($46 \times 162\,\mu m^2$), 92 nm by step, (Gwyddion software). Note that A indicates the orientation of the scanned zone.

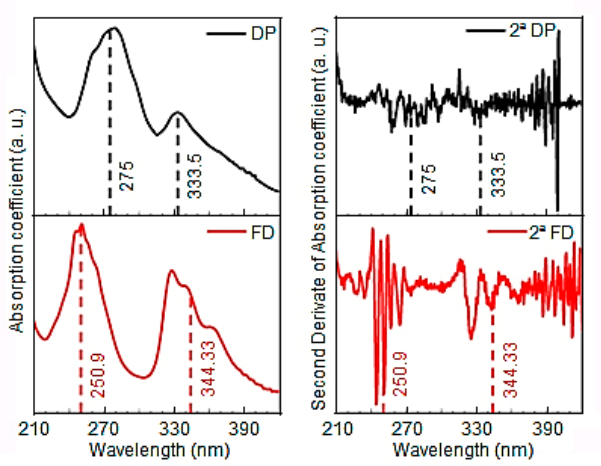

Figure 3. a) Absorption spectrum of KBr: Eu^{2+} a single crystal in bulk in free dipoles state (-FD), and dihalide phase state (-DP); b) Second derivative of the absorption spectra; free dipoles (- 2a FD) and dihalide phase (- 2a DP) states.

aggregates) correlated emission band is the only one that remains after cooling the sample to 500 °C. Europium ions are evenly distributed in the host; only one emission band peaking at $418\,nm$ (FWHM, $0.08\,eV$) is present. The other emission spectrum is from the sample in DP, whose heat treatment to achieve this phase was previously mentioned. This emission band becomes wide and presents a positive Gaussian asymmetric distribution, with a

principal peak at 429.8 nm and a shoulder peak at about 466.2 nm. The deconvolution of the emission spectrum of europium ions configured in the DP at room temperature was performed using Origin 2017 (OriginLab Corporation, USA). The red line refers to the convolution fit of the entire emission spectrum. The "Peak Analyzer" tool assists in the process of separating overlapping peaks, identifying three distinct bands. One at 418 nm, with a FWHM of 0.05 eV and 0.14 $a.u.$ of total intensity. This band indicates that there are remnants of europium ions that have not participated in the formation of any phase (Hernández et al., 1980). One band at 429.8 nm, with a FWHM of 0.19 eV and 0.93 $a.u.$ of total intensity, which is associated with the SDP, and it is known as the coherent phase with the host because it does not deform the crystal field, unlike the second component at 466.2 nm with a FWHM of 0.27 eV and 0.46 $a.u.$ of total intensity. That is associated with the MDP, which is inconsistent with the host and distorts it (Muñoz-Santiuste et al., 1990; Aguilar et al., 1982). These results suggest that the crystal field at the Eu^{+2} site is larger when the impurity is dispersed into the lattice.

Figure 5 shows the schematic of the absorption, excitation, and emission process of divalent europium in DP obtained by the *step-by-step* scanning method. In Figure 5a, the optical absorption spectra from $KBr{:}Eu^{2+}$ in DP; it has two bands associated to transitions from the $4f^7(^8S_{7/2})$ ground state to the t_{2g} (low energy band) and e_g (high energy band) components of the $4f^6 5d$ in the excited state (Hernández et al., 1980). It is known that when excitation occurs in either of these two bands, an emission band is produced. Its position and shape are directly related to the thermal history and the components of the host that contain it (Hernández et al., 1980; Muñoz-Santiuste et al., 1990; López et al., 1980; Poort et al., 1997). Any reconfiguration in the crystalline environment causes changes in the $4f^6 5d^1$ transition because the 5d energy level is exposed to the outer layer. Figure 5b shows three main emissions associated with: E at λ = 418 nm, FD, $E1$ = ~ 424.7 nm, SDP with blue emission, and $E2$ = ~ 469.2 nm, MDP with cyan emission (Muñoz-Santiuste et al., 1990; Mejía-Uriarte et al., 2009; Aguilar et al., 1982).

The microsample (insert in Figure 6) was scanned to determine the luminescent response of its different areas. It was observed that the shape, peak position, and intensity of the emission spectra changed according to the position of the microscope objective on the micro-sample along the $\boldsymbol{X}$ and $\boldsymbol{Y}$ axes. In this process, three main types of emission bands were observed with different shapes corresponding to the distribution: asymmetric Gaussian, Gaussian, and double Gaussian.

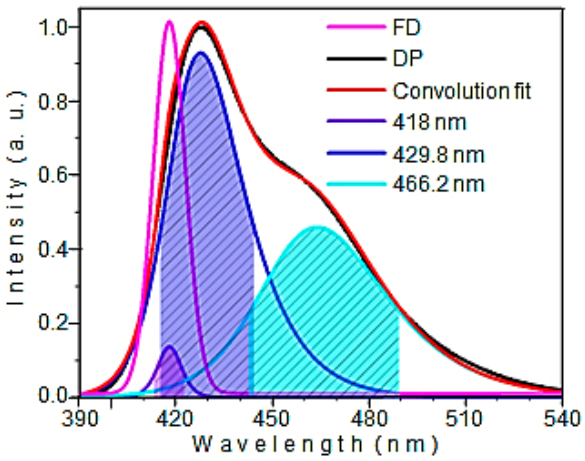

Figure 4. Normalized emission spectrum of $KBr{:}Eu^{2+}$ ($4f^6 5d^1 \rightarrow 4f^7$ transition of Eu^{2+}) of the single crystal in bulk under laser excitation 375 nm at room temperature. Sample in - FD and deconvolution of the emission spectrum of -**DP**, into three emission peaks by Gaussian fitting.

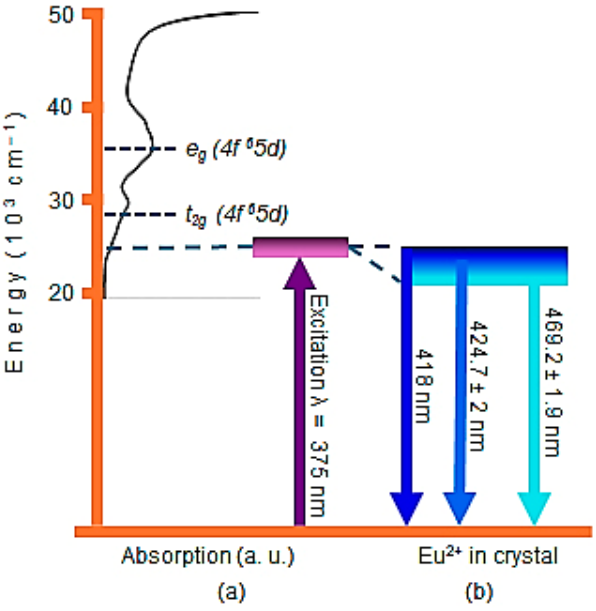

Figure 5. a) Absorption spectrum of a sample in the dihalide phase. b) Energy level of Eu^{2+}.

Figure 6 illustrates the emission spectrum obtained at six points (P_1,..., P_6) on the sample, using the same excitation wavelength of a 375 nm laser beam. It has a nonuniform thickness, with the left end thicker than the right, revealing areas of greater luminescence on the left. The emission spectra were collected at six points: P_1 (center) and P_2 (lower left corner), are almost identical, and

there is only a $0.5\,nm$ peak shift of the P_2 concerning P_1; this could be related to the diameter of the NS in SDP, just like the NS in Suzuki phase formed in this type of material (Mejía-Uriarte et al., 2009). The two spectra exhibit a similar asymmetric Gaussian distribution, predominantly showing the blue band associated with SDP at a wavelength of $424\,nm$, alongside a minor component from the cyan band of MDP at ~ $470\,nm$. When only one emission band is present, as P_3, P_5, and P_6 points indicate that at that point NS are configured only in the SDP and their emission spectrum corresponds to a symmetric Gaussian distribution. The peaks shifted from ~ $423\ to\ 424\,nm$; this may be due to the diameter of the NS, previously mentioned. And approximately $0.13\,a.u.$ of intensity between them; these changes are related to the number and thickness of each of them due to a greater number of emitting ions. The emission spectrum at the P_4 point was observed to have an asymmetric Gaussian distribution with a greater contribution from the MDP (Aguilar et al., 1982). Scanning around this point, significant spectral changes between steps were observed, demonstrating the simultaneous presence of both phases (SDP and MDP). When scanning, it was observed that at each step, the emission spectra show changes; in some cases, only small shifts in the position of the emission peak or the intensity are seen, but the spectra collected around this point, P_4 have a strong emission from the second band related to the MDP. Therefore, a rectangular area was chosen for the detailed study, SZ.

The $\boldsymbol{XY}$ motorized plates passed $92\,nm$ each step and remained stationary at each point for $20\,ms$. This movement was synchronized with the spectrometer to facilitate the collection of the emission spectrum at each predetermined position. The resolution determined by the Rayleigh criterion is $254.16\,nm$, while the depth of the field is approximately $100\,nm$. A motorized component along the $\boldsymbol{Z}$-axis, with a step size of $50\,nm$, was employed to position the optical focus accurately. This was achieved by adjusting the orientation of a mirror until the maximum response of the photodiode was obtained. The light was collected at stationary points every $92\,nm$ along both axes, with the scan conducted along the $\boldsymbol{Y}$-axis over $162\,\mu m$.

Figure 7 presents a 3D image that shows the terrace characteristics of alkali halides in the reconstructed image of the sample surface. Only particular protuberances can be observed, likely indicating the presence of precipitate in that area. Unfortunately, the software used was unable to measure the height of the terraces. Their height was determined using the AFM images shown below. In

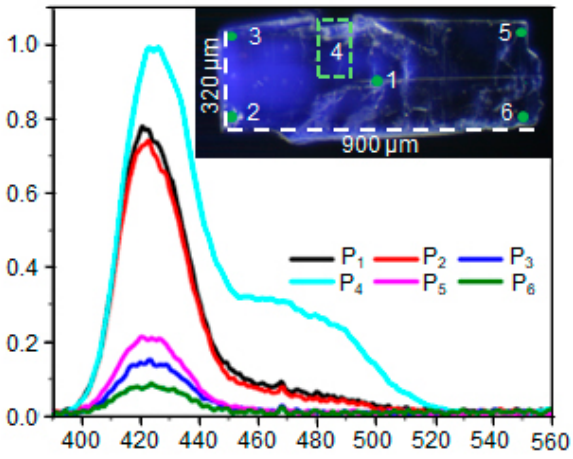

Figure 6. Micro-sample, $900 \times 320\ \mu m^2$. Points P_1 to P_6 represent the locations where emission spectra are collected, $\lambda_{exc} = 375\,nm$. Insert image: dotted rectangle, around P_4, SZ.

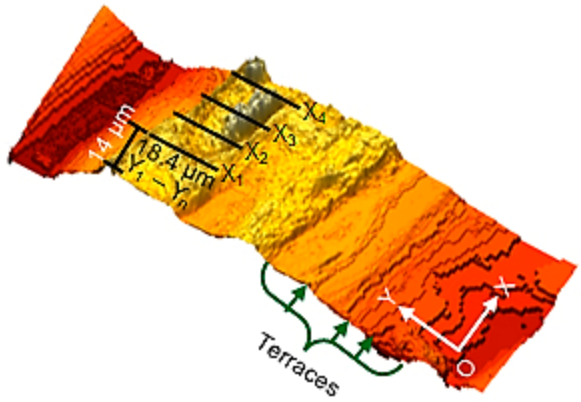

Figure 7. Image 3D from the surface of one section, $46 \times 162\ \mu m^2$ (SZ) at different positions of the crystal edge scanned (left), $\boldsymbol{X}_1$: $14\,\mu m$, $\boldsymbol{X}_2$: $24\,\mu m$, $\boldsymbol{X}_3$: $34\,\mu m$, and $\boldsymbol{X}_4$: $44\,\mu m$. The scan is on the $\boldsymbol{Y}$ axis, $18.4\,\mu m$. (Gwyddion software).

Supplementary Materials (SM), other zones are presented (Figure S1, S2, and S3). The 3D images were obtained using the Gwyddion software, which enables the analysis of various microscopy techniques, including SPM, AFM, SNOM, and others. To visualize 3D images, it uses an OpenGL 3D data display, which uses a false-color or material representation, easily editable color maps, and OpenGL materials (Nečas & Klapetek, 2012).

The spectra were collected in all SZ; here, it shows four scans at positions $\boldsymbol{X}_{1\text{-}4}$ and scanned at $\boldsymbol{Y}_{1\text{-}n}$, $n = 200$ spectra. The SZ was $500\,(\boldsymbol{X}) \times 1760\,(\boldsymbol{Y})$, equivalent to

$46 \times 162\ \mu m^2$, and *1760* emission spectra were collected for each line in the $\boldsymbol{Y}$ axis. Consequently, only the spectra from the region with the highest intensity exchange between the $E1$ and $E2$ bands were selected to show 200 emission spectra over $18.4\ \mu m$. The microscope objective collects the emitted photons from the laser beam focus area; this way, the luminescence of the NS is obtained. The peaks of the emission bands shift and change in intensity, even disappearing and reappearing after being displaced by only a few tens of nanometers. These changes are related to the quantity, diameter, and thickness of the NS in SDP and/or MDP found at each step, keeping in mind that the sample is approximately 90 m thick and there is enough space for thousands of NS. Throughout the scanning of the sample, it is possible to observe the coexistence of NS in both phases. Thus, the shape of the emission spectrum depends on the number of NS in each phase. Therefore, the emission spectrum corresponds to a positively or negatively asymmetric Gaussian distribution depending on whether NS are present in the SDP or MDP, respectively. When the number of NS is proportional in both phases, the emission spectrum exhibits a double Gaussian distribution. Blue emission predominated in most of the samples, but there was an area where cyan emission was greater than blue; this area was analyzed and shown in Figure 8. The changes in real-time can be seen in Supplementary Material videos (VS1 and VS2).

Figure 8 (a) illustrates the scan taken $14\ \mu m$ from the origin in the X direction. The E1 and E2 bands exhibit intensity variations of approximately between 0.25 and 0.34 *a.u.*, respectively.

These modifications could be associated with changes in quantity and so as size of NS in the micro-sample. The increase in the $E2$ band is attributed to the higher concentration of NS in MDP. The insert showed that every 30 steps (equivalent to 2.76 μm), the $E1$ band remains nearly stable in both intensity and wavelength. In contrast, the $E2$ band intensifies, resulting in the formation of a second emission band. The collection of the luminescent response obtained *step-by-step* allowed us to locate the type of NS that are emitting at each point. Figure 8 (b), at $24\ \mu m$ ($\boldsymbol{X}_2$ line), presents an interesting behavior, as the

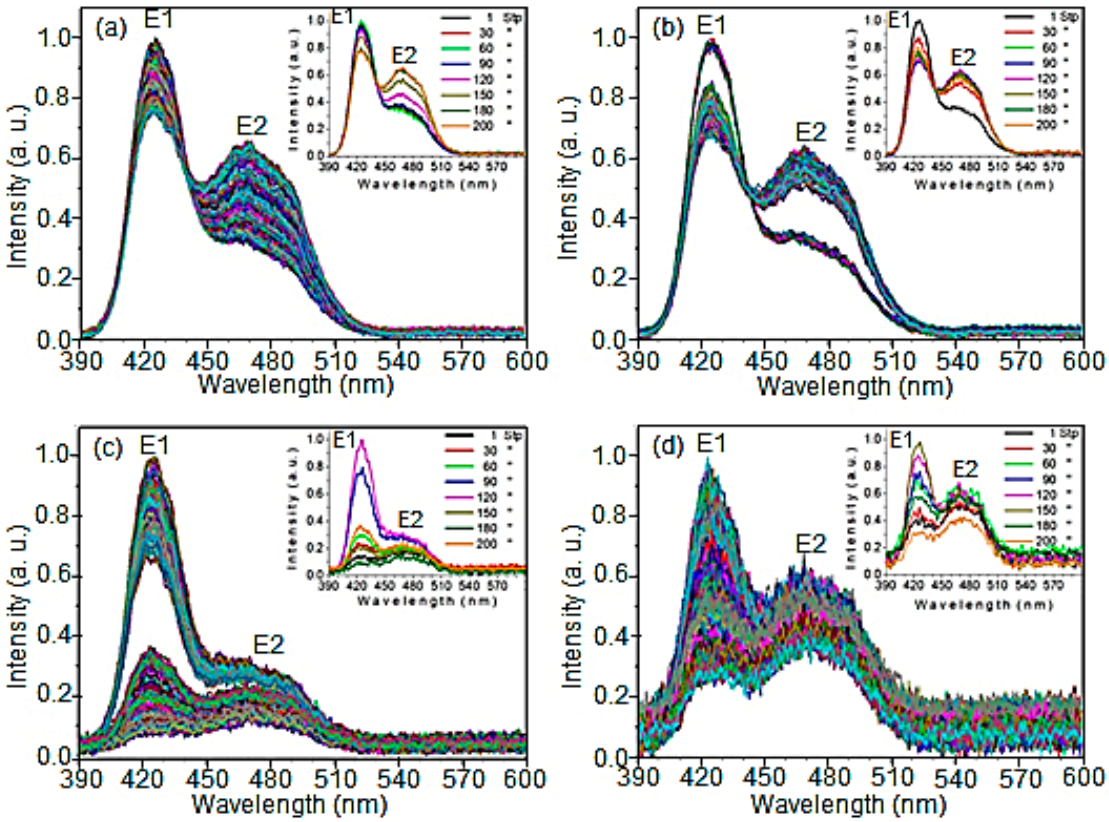

Figure 8. Two hundred emission spectra at several positions along the $\boldsymbol{X}$ axis were scanned $18.4\ \mu m$ over the $\boldsymbol{Y}$ axis, each 92 nm by step. Scan in $\boldsymbol{X}$ axis at a) $\boldsymbol{X}_1$, 14 μm, b) $\boldsymbol{X}_2$, 24 μm, c) $\boldsymbol{X}_3$, 34 μm, d) $\boldsymbol{X}_4$, 44 μm. The insert in the figure is every 30 steps, which corresponds to 2.76 μm.

intensities of the $E1$ and $E2$ bands exhibit minimal variation $0.06\ a.u.$ During their path of $2.76\ \mu m$, there is almost no significant change, but over the next 15.64 microns, the intensity of the $E1$ and $E2$ bands change by 0.19 and $0.15\ a.u.$, respectively, as shown in the figure insert. From spectrum 35 to 36, by shifting only $92\ nm$, the shape of the emission band changes from a double Gaussian to a positively asymmetric Gaussian distribution. The intensity at each point exhibits variability; it may be greater or less than the preceding or following points. Furthermore, certain regions along the path may demonstrate shifts in wavelength while preserving the overall shape of the spectral band. This can be detected by the field of focus and depth of focus of the laser beam. In Figure 8 (c), it is observed that the emission bands $E1$ and $E2$ show an increase and decrease in intensity at each step. But there is a region from the 78 to the 126 step where the $E1$ band increases its intensity more than the $E2$ band, giving rise to an "opening" in the sequence of spectra. The collection of emissions indicates that there are more NS in SDP in that $\boldsymbol{X}_3$ line. As the trajectory progresses, the E1 band decreases until the E2 band becomes predominant, as shown in the inset graph. It can be observed that from step 1 (-) to step 120 (-), the $E1$ band intensifies significantly, losing its double Gaussian shape and transforming into a positive asymmetrical Gaussian distribution. Subsequently, at step 150 (-), it reverts to its previous state. At $18.4\ \mu m$ of travel, two emission bands alternate in intensity between $E1$ and $E2$, however, the presence of both emission bands remains. It is essential to note that the $E2$ band becomes more intense only when the $E1$ band almost disappears, thereby allowing the luminescence of the $E2$ band to become more prominent. This observation suggests that the largest NS is present in the MDP, and very few NS in the SDP are in the same area. These changes are not necessarily sequential, indicating that at each $92\ nm$ increment, a variety of types or sizes of NS are detected. The $E2$ band showed its most substantial contribution $44\ \mu m$ from the edge of the scan (Figure 8 (d)). In this area, there is competition between the $E1$ and $E2$ bands, with significant fluctuations in intensity directly linked to the random distribution of the NS formed in both phases. In the insert of the same figure, to $18.4\ \mu m$ of travel, the two emission bands are discerned, alternating the intensity of the bands in $E1 \geq E2$ or $E1 \leq E2$, but always maintaining the double emission. In particular, the E2 band shows greater intensity with respect to the E1 band only when the latter has decreased, thereby allowing the luminescence of the $E2$ band to become more prominent. The image obtained by light scanning (Fig. 7) shows bulges on the surface and more specifically from $\boldsymbol{X}_1$ to $\boldsymbol{X}_4$. These irregularities are likely related to a greater presence of NS in the MDP. Notable changes were observed in the intensity, shape, and position of the emission spectrum. The supplementary material shows a path 36.8 µm (equivalent to 400 spectra) after the 18.4 µm path shown in Figure 8. The strong presence of the E2 band is still detected in this region (see SM graphs FS4, FS5, FS6, and FS7).

Figure 9 presents the main changes in emission spectra recorded in the scanning process along $18.4\ \mu m$ from Figure 8 (d) $44\ \mu m$ in $\boldsymbol{X}_4$. To prevent the graph from becoming saturated, a selection of 100 spectra was made, with samples taken at every two steps, equivalent to $184\ nm$ (in SM, the Tables TS1 and TS2 are shown with the data). The $E1$ band has $\bar{\lambda}_{\mathrm{E1peak}} = 424.7$ nm (from 420.9 to 429.4 nm) with $\sigma = 2\ nm$. As mentioned previously, the position of the emission band peak is related to the diameter of the NS. In this case, there is a high degree of dispersion in the diameter of the NS in SDP, and its intensity has 68% variability. The E2 band has $\bar{\lambda}_{\mathrm{E2peak}} = 469.2\ nm$ (from 465.5 to $478.6\ nm$) and $\sigma = 1.9\ nm$, with mode value at $468.7\ nm$. There are some spectra with peak positions around this value, but they are mainly shifted to longer wavelengths. Taking as a reference the effect of the diameter of the NS on the position of the emission peak, this result could be interpreted as that of most NS that are in MDP have a similar diameter, and the intensity of this band presents a variability of ~24.4% of the collected light, which is less than the variation of the $E1$ band. In step 148, the $E1$ band is larger than the $E2$ band (---), with 32% more intense than the $E2$ band, which corresponds

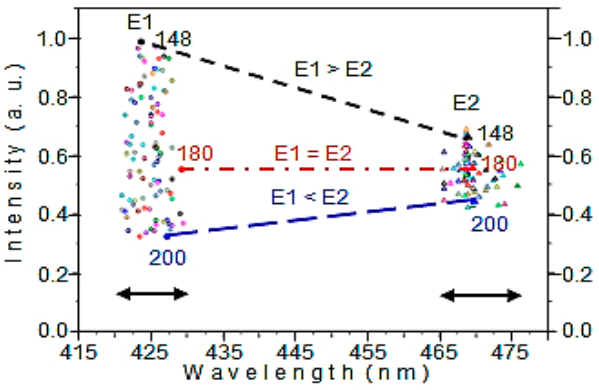

Figure 9. The analysis of the emission spectra (peak and wavelength) of Figure 8(d) is shown at every two steps of $92\ nm$ each one. $E1 > E2$ (---) step **148**, $E1 = E2$ (·) step **180**, and $E1 < E2$ (– –) step **200**.

to a spectrum close to step 150 shown in the insert of Figure 8 (d). The line (·) represents the condition when $E1$ equals $E2$ in step 180 ($Y = 16.56\ \mu m$), and shows an emission spectrum with a double Gaussian distribution of equal intensity. The line (– –) indicates that $E1$ is less than $E2$ in step 200 ($\boldsymbol{Y} = 18.4\ \mu m$). In this position, the $E2$ band has 12% more intensity than the $E1$ band, and its emission spectrum tends towards a negative, asymmetric Gaussian distribution.

To understand the emission spectra and their relationship with different types of NS, Figure 10 illustrates the deconvolution of the luminescence bands for the micro-sample from Figure 7. The scan reveals several areas with an asymmetric Gaussian distribution (see Figure 10 (a), representative graph). The primary emission occurs around $424.7\ nm$ ($E1$, SDP), with a secondary component at $469.2\ nm$ ($E2$, MDP) that has low intensity, typically ranging from $10 - 30\%$ of the total intensity of the $E1$ band.

The emission band observed $418\ nm$ corresponds to the FD (FWHM, $0.09\ eV$) present in the crystal, and during the annealing treatment, this band decreases, giving rise to the formation of DP in samples. The spectrum consistently exhibits this form of asymmetric Gaussian distribution (Muñoz-Santiuste et al., 1990; Aguilar et al., 1982). The scan performed $\boldsymbol{X}_4$ presents a double Gaussian distribution in most of the path. In Figure 10 (b), $E2$ the intensity of the $E1$ band. Figure 10 (c) reveals that the enveloping curve represents the combined intensity of the $E1$ and $E2$ bands. The intensity of the bands is similar, which indicates that in that area, there are NS in SDP and MDP in similar quantities. However, deconvolution analysis indicates that the $E2$ band has already surpassed the $E1$ band, suggesting a higher presence of NS in MDP, corresponding to FWHM values of 0.18 and $0.3\ eV$ for $E1$ and $E2$ bands, respectively.

The area where the $E2$ band is dominant is shown in Figure 10(d). There are intervals where the $E2$ band exceeds the $E1$ band in intensity up to 27%. Nevertheless, deconvolution analysis indicates that the contribution of the $E1$ band is comparatively lower with 0.17 and $0.3\ eV$ as the value of the FWHM in $E1$ and $E2$, respectively. As the intensity of the $E1$ band decreases, the profile of the $E2$ band becomes noisy. This is most noticeable when the intensities of the bands are equal and when $E2$ band is greater than $E1$. This phenomenon could be related to the previously reported vibronic behavior (Pérez-Salas et al., 2003). Here, we demonstrate that both phases coexist and are randomly distributed within the crystal. The changes in emission intensity are attributed to the

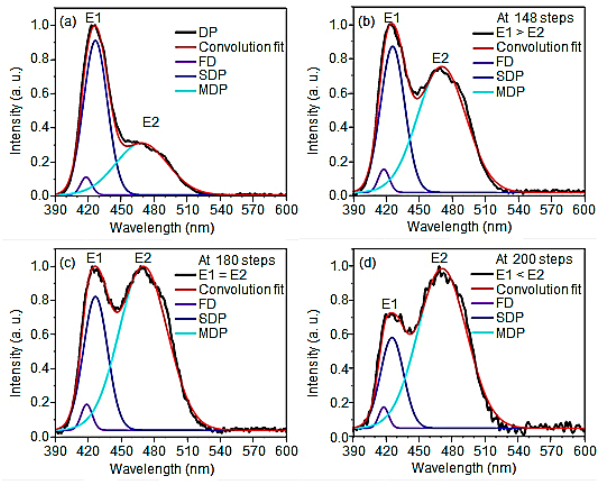

Figure 10. Deconvolution of localized emission spectra; a) In areas where the luminescent response has an asymmetric distribution. Double Gaussian distribution in $\boldsymbol{X}_4$ line; b) At 148 step, $E1 > E2$, c) At 180 step, $E1 = E2$ and d) At 200 step, $E1 > E2$. Collected spectrum (-), convolution fit (-), free dipoles with peak at $418\ nm$ (-), SDP ($427.7\ nm$, (-), MDP ($469.2\ nm$ (-).

quantity of NS in SP or MDP. The sample was analyzed by AFM to observe the shape and distribution of the NS. The scan area around the $\boldsymbol{X}_4$ line was chosen because of the $E2$ band had a higher intensity than the $E1$ band. The area was located using reference marks in the image and spectrum collection from Figure 7. The resulting AFM image, shown in Figure 11, reveals two distinct NS shapes within the crystal. The first is a *circular disc type* with a diameters $< 80\ nm$ and a maximum height of $1\ nm$. The second type is *irregular lamellar*, with values exceeding $80\ nm$; some reach diameters of up to $200\ nm$ and even $330\ nm$, with a maximum height of up to $2.5\ nm$ measured from the surface. The height of the NS has not been precisely determined because part of it is embedded within the host. The single crystal has wide atomic flat terraces with a height of $0.3289\ nm$, which is half of the lattice constant, $0.6578\ nm$, on the $[100]$ direction for the KBr single crystal (Mejía-Uriarte et al., 2009). In our case, the terrace profile of the KBr: Eu^{2+} single crystal (shown in the same figure) has a height of $0.325\ nm$, the lowest value found. The average terrace height is $0.375\ nm$, and the highest value was $0.425\ nm$. It should be noted that when growing NS on the terraces, they distort the lattice, so the heights between terraces vary. Terraces are generally flat with low-energy regions; for this reason, NS tend to grow at their edges. By obtaining the AFM image of the micro-sample in the area where the $E1$ band is more intense than the $E2$ band, it was found that most NS are small

(see Fig. S8). The largest NS are mainly found between terrace levels, making them unstable and incoherent with the host. From the results obtained, emission spectra and AFM images, and in agreement with the reported literature, we can associate the small NS with the SDP and the larger NS with the MDP. When the sample is heated, the $E2$ band is the first to disappear at $230\,°C$, indicating that it tends to fracture when the host is distorted due to temperature. Due to its characteristics, it is associated with the MDP. In contrast, the $E1$ band remains stable up to above $260\,°C$, and is related to the SDP (Aguilar et al., 1982).

Figure 11 shows that the emission spectra change continuously as the laser beam scans over the sample surface. In each point examined, a different emission spectrum is generated based on the specific type of nanostructure found. Epifluorescence analysis of alkali halide samples reveals distinct NS formed within the host via precipitation and aggregation, particularly upon heat treatments or extended annealing at room temperature (Cordero-Borboa & Jiménez-García, 2005).

Conclusions

Emission spectra were detected using a step-by-step light-scanning method. The luminescence bands exhibited three types of distribution: 1) Asymmetric Gaussian distribution ($424.7\,nm$ and a component at $469.2\,nm$), suggesting the presence of NS in SDP and MDP, coherent and incoherent with the host, respectively. In this case, stable nanostructures are predominant. 2) Symmetric Gaussian distribution ($424.7\,nm$) shows the presence of nanostructures exclusively in SDP. 3) Double Gaussian distribution ($424.7\,nm$ and $469.2\,nm$), indicating that NS coexist in both phases. SDP is coherent with the host and has been reported previously, whereas MDP is less well-known and typically appears as a component of the emission band. Samples stored for six months at temperatures $\geq to\,200\,°C$, exhibit multiphoton emission from the higher excited state to the lower excited state, with an emission range of approximately $390\,nm$ to $525\,nm$. These Eu^{2+} ions emissions originated from $4f^6 5d^1 \rightarrow 4f^7$ electronic transition inside of NS of different sizes and configurations. This double emission of Eu^{2+} in the KBr host, specifically a blue and cyan band at room temperature, has been demonstrated.

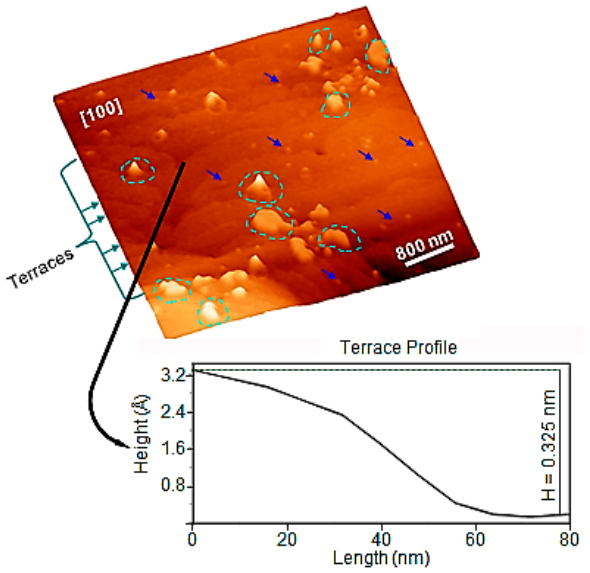

Figure 11. AFM imagen of KBr: Eu^{2+}, $4 \times 4\ \mu m^2$. NS of different sizes can be observed. Here, the blue rows indicate a *circular disc type* of NS (diameter < $80\,nm$), while the circular shape in cyan indicates NS with *irregular lamellar* (diameter > $80\,nm$). The terrace profile shows the unevenness of the single crystal, with a height of approximately half the network parameter, $0.325\,nm$ (Wakaki et al., 2007).

Acknowledgements

We appreciate the technical support from Raúl Ruvalcaba Morales, Sergio Padilla, and Roberto Hinojosa Nava.

In tribute to José Manuel Hernández for his career and retirement, and In Memory of Héctor Murrieta, thank you for sharing your knowledge.

Funding

The authors acknowledge the support of PAPIIT projects IT102323 and IN110224, the Programa de Maestría y Doctorado en Ingeniería-UNAM, and CONAHCYT for the fellowship received.

Conflict of Interest

The authors declare that they have no conflicts of interest to disclose.

References

Aguilar G., M., Rubio O., J., López, F. J., García-Solé, J., & Murrieta, H. S. (1982). Optical absorption and fluorescence investigation of the precipitated phases of Eu^{2+} in KBr single crystals. *Solid State Communications*, *44*(2), 141–144. https://doi.org/10.1016/0038-1098(82)90417-3.

Barth, C., & Henry, C. R. (2009). NaCl (001) surfaces nanostructured by Suzuki precipitates: a scanning force microscopy study. *New Journal of Physics*, *11*(4), 043003. https://doi.org/10.1088/1367-2630/11/4/043003

Cordero-Borboa*, A. E., & Jiménez-García, L. F. (2005). Epifluorescence optical microscopy: a sensitive tool for determining the spatial distribution of europium-dihalide precipitates in KCl: KBr: Eu2+ crystals. *Philosophical magazine letters*, *85*(7), 345-357. https://doi.org/10.1080/09500830500229378.

da Cunha Andrade, L. H., Lima, S. M., da Silva, R. V., Baesso, M. L., Guyot, Y., & Nunes, L. A. D. O. (2014). White-light-emitting KCl: Eu2+/KCN crystal for solid-state lighting devices. *Journal of Materials Chemistry C*, *2*(47), 10149-10156. https://doi.org/10.1039/c4tc01190b.

de Carcer, I. A., Cussó, F., & Jaque, F. (1988). Afterglow and photoconductivity in europium-doped alkali halides. *Physical Review B*, *38*(15), 10812. https://doi.org/10.1103/physrevb.38.10812.

Dorenbos, P. (2003). Energy of the first 4f7→ 4f65d transition of Eu2+ in inorganic compounds. *Journal of luminescence*, *104*(4), 239-260. https://doi.org/10.1016/s0022-2313(03)00078-4.

Duan, C. K., & Reid, M. F. (2003). A simple model for f→ d transitions of rare-earth ions in crystals. *Journal of Solid State Chemistry*, *171*(1-2), 299-303. https://doi.org/10.1016/s0022-4596(02)00181-0.

Eick, H. A., & Smeggil, J. G. (1971). Crystal structure of strontium dibromide. *Inorganic Chemistry*, *10*(7), 1458-1460. https://doi.org/10.1021/ic50101a028.

Galimov, D. I., Yakupova, S. M., Vasilyuk, K. S., & Bulgakov, R. G. (2020). Bright two-color halogen-dependent chemiluminescence of Eu2+* ions at the oxidation of organoaluminium compounds by oxygen in the presence of europium dihalides. *Journal of Photochemistry and Photobiology A: Chemistry*, *397*, 112587. https://doi.org/10.1016/j.jphotochem.2020.112587.

Henderson, B., & Imbusch, G. F. (2006). Spectroscopy of lanthanide (rare-earth) and actinide ions in solids. En *Optical Spectroscopy of Inorganic Solids* (pp. 387–407). Oxford University Press Oxford.

Hernández A., J., Cory, W. K., & Rubio O., J. (1980). Optical investigation of divalent europium in the alkali chlorides and bromides. *The Journal of Chemical Physics*, *72*(1), 198–205. https://doi.org/10.1063/1.438875.

Horcas, I., Fernández, R., Gómez-Rodríguez, J. M., Colchero, J. W. S. X., Gómez-Herrero, J. W. S. X. M., & Baro, A. M. (2007). WSXM: A software for scanning probe microscopy and a tool for nanotechnology. *Review of scientific instruments*, *78*(1). https://doi.org/10.1063/1.2432410.

Hossain, M. K., Ahmed, M. H., Khan, M. I., Miah, M. S., & Hossain, S. (2021). Recent progress of rare earth oxides for sensor, detector, and electronic device applications: A review. *ACS Applied Electronic Materials*, *3*(10), 4255–4283. https://doi.org/10.1021/acsaelm.1c00703.

Huang, J., Lei, T., Siron, M., Zhang, Y., Yu, S., Seeler, F., ... & Yang, P. (2020). Lead-free cesium europium halide perovskite nanocrystals. *Nano Letters*, *20*(5), 3734-3739. https://doi.org/10.1021/acs.nanolett.0c00692.

Kunkel, N., Rudolph, D., Meijerink, A., Rommel, S., Weihrich, R., Kohlmann, H., & Schleid, T. (2015). Green luminescence of divalent europium in the hydride chloride EuHCl. *Zeitschrift für anorganische und allgemeine Chemie*, *641*(7), 1220-1224. https://doi.org/10.1002/zaac.201400531.

Kuzmin, V. I., Paramonov, A. A., Tytik, D. L., & Souvorova, O. V. (2024). Method for Analysis of Asymmetric Spectra Based on the Information Entropy Model. *Physics of Wave Phenomena*, *32*(3), 203-208. https://doi.org/10.3103/s1541308x24700171.

López, F. J., S., H. M., A., J. H., & O., J. R. (1980). Optical absorption and luminescence investigations of the precipitated phases of Eu^{2+} in $NaCl$ and KCl single crystals. *Physical Review. B, Condensed Matter*, *22*(12), 6428–6439. https://doi.org/10.1103/physrevb.22.6428

López, F. J. (1981). Addendum to" Optical absorption and luminescence investigations of the precipitated phases of Eu 2+ in NaCl and KCl single crystals". *Physical Review B*, *24*(8), 4847. https://doi.org/10.1103/physrevb.24.4847.

Luo, J., Yang, L., Tan, Z., Xie, W., Sun, Q., Li, J., Du, P., Xiao, Q., Wang, L., Zhao, X., Niu, G., Gao, L., Jin, S., & Tang, J. (2021). Efficient blue light emitting diodes based on europium Halide perovskites. *Advanced Materials (Deerfield Beach, Fla.)*, *33*(38), e2101903. https://doi.org/10.1002/adma.202101903.

Mejía-Uriarte, E. V., Bañuelos, J. G., Kolokoltsev, O., Navarrete, M., Jaque, F., & Camarillo, E. (2009). Influence of europium nanostructure size on the emission of KBr: Eu^{2+}. *Solid State Communications*, *149*(11-12), 445-447. https://doi.org/10.1016/j.ssc.2008.12.042.

Mejía-Uriarte, E. V., Castañeda-Guzmán, R., Villagrán-Muniz, M., Camarillo, E., & Navarrete, M. (2003). Studies of the thermal dissolution process of the Suzuki phase of the Eu2+ ion in KBr single crystals by analysis of photoacoustic signals. *Journal of Physics: Condensed Matter*, *15*(40), 6889-6898. https://doi.org/10.1088/0953-8984/15/40/024.

Mejía-Uriarte, E. V., Kolokoltsev, O., Montesinos, M. N., & Camarillo, E. (2015). Study of NaCl: Mn2+ nanostructures in the Suzuki phase by optical spectroscopy and atomic force microscopy. *Journal of Luminescence*, *160*, 293-298. https://doi.org/10.1016/j.jlumin.2014.12.015.

Muñoz-Santiuste JE, Garca Solé J, & Manfredi, M. (1990). Precipitation-induced quenching of Eu^{2+} luminescence in potassium halides. *Physical Review. B, Condensed Matter*, *42*(17), 11339–11344. https://doi.org/10.1103/physrevb.42.11339.

Nečas, D., & Klapetek, P. (2012). Gwyddion: an open-source software for SPM data analysis. *Central European Journal of Physics*, *10*(1), 181-188. https://doi.org/10.2478/s11534-011-0096-2.

Nikl, M., & Yoshikawa, A. (2015). Recent R&D trends in inorganic single-crystal scintillator materials for radiation detection. *Advanced Optical Materials*, *3*(4), 463-481. https://doi.org/10.1002/adom.201400571.

Pérez-Salas, R., Meléndrez, R., Aceves, R., Rodriguez, R., & Barboza-Flores, M. (1996). Room-temperature effects of UV radiation in KBr: crystals. *Journal of Physics: Condensed Matter*, *8*(27), 4983-4992. https://doi.org/10.1088/0953-8984/8/27/009.

Pérez-Salas, R., Piters, T. M., Aceves, R., Rodríguez-Mijangos, R., & Barboza-Flores, M. (2003). Optical vibronic spectra of aggregates in Eu2+-doped KCl and KBr crystals. *Revista mexicana de fisica*, *49*(2), 102-106. https://www.scielo.org.mx/scielo.php?pid=S0035-001X2003000200001&script=sci_arttext&tlng=en

Poort, S. H. M., & Blasse, G. (1997). The influence of the host lattice on the luminescence of divalent europium. *Journal of Luminescence*, *72*, 247-249. https://doi.org/10.1016/s0022-2313(96)00360-2.

Qiao, J., Zhang, S., Zhou, X., Chen, W., Gautier, R., & Xia, Z. (2022). Near-infrared light-emitting diodes utilizing a europium-activated calcium oxide phosphor with external quantum efficiency of up to 54.7%. *Advanced Materials*, *34*(26), 2201887. https://doi.org/10.1002/adma.202201887.

Qin, X., Liu, X., Huang, W., Bettinelli, M., & Liu, X. (2017). Lanthanide-activated phosphors based on 4f-5d optical transitions: theoretical and experimental aspects. *Chemical reviews*, *117*(5), 4488-4527. https://doi.org/10.1021/acs.chemrev.6b00691.

Solak, A. C., Royer, L. A., & Janhangeer, A. R. (2022). Kobayashi, H. royerlab/aydin: v0. 1.15. *Zenodo https://doi.org/10.5281/zenodo*, *5654826*. https://doi.org/10.5281/zenodo.7222198

Stand, L., Zhuravleva, M., Chakoumakos, B., Wei, H., Johnson, J., Martin, V., Loyd, M., Rutstrom, D., McAlexander, W., Wu, Y., Koschan, M., & Melcher, C. L. (2019). Characterization of mixed halide scintillators: $CsSrBrI_2$: Eu, $CsCaBrI_2$: Eu and $CsSrClBr_2$: Eu. *Journal of Luminescence*, *207*, 70–77. https://doi.org/10.1016/j.jlumin.2018.10.108.

Stepien-Damm, J., & Dubiel, M. (1980). Effect of Eu2+ concentration on the lattice parameter and density of KCl crystals. *physica status solidi (a)*, *59*(2), 743-747. https://doi.org/10.1002/pssa.2210590241.

Wakaki, M., Shibuya, T., & Kudo, K. (2007). *Physical properties and data of optical materials* (M. Wakaki, Ed.). https://doi.org/10.1201/9781420015508.

Weakliem, H. A. (1972). Electronic Interactions in the 4 f 6 5 d Configuration of Eu 2+ in Crystals. *Physical Review B*, *6*(7), 2743. https://doi.org/10.1103/physrevb.6.2743.

Wu, M., Deng, D., Ruan, F., Chen, B., Lei, L., Lei, R., & Xu, S. (2019). Double-site emission of Eu2+ ions in Sr4Al14O25: Eu2+ phosphors for self-calibrated optical thermometry. *Optical Materials*, *88*, 704-710. https://doi.org/10.1016/j.optmat.2018.12.058.

Wu, Y., Gokhale, S. S., Lindsey, A. C., Zhuravleva, M., Stand, L., Johnson, J. A., II, Loyd, M., Koschan, M., & Melcher, C. L. (2016). Toward high energy resolution in $CsSrI_3/Eu^{2+}$

scintillating crystals: Effects of off-stoichiometry and Eu^{2+} concentration. *Crystal Growth & Design*, *16*(12), 7186–7193. https://doi.org/10.1021/acs.cgd.6b01375.

Yuan, H., Jin, S., Zheng, S., Xie, R., Pang, T., Zhuang, B., ... & Chen, D. (2024). Nanocrystals of divalent europium-doped CsPbCl3 perovskites: a novel optoelectronic material with dual-emissions. *Journal of Materials Chemistry C*, *12*(4), 1430-1439. https://doi.org/10.1039/d3tc04288j.

Zhang, Y., Chen, L., Wang, X., Liu, W., & Wang, S. (2024). Europium-bearing organic framework with excellent X-ray scintillating luminescence. *Journal of Rare Earths*, *42*(2), 251–255. https://doi.org/10.1016/j.jre.2023.07.015.

Zhao, X., Fu, P., Li, P., Du, H., Zhu, J., Ge, C., Yang, L., Song, B., Wu, H., Jin, T., Guo, Q., Wang, L., Li, J., Xiao, Z., Chang, J., Niu, G., Luo, J., & Tang, J. (2023). Solution-processed hybrid europium (II) iodide scintillator for sensitive X-ray detection. *Research (Washington, D.C.)*, *6*, 0125. https://doi.org/10.34133/research.0125.